Supplementary Materials for “ Efficient Test-Time Adaptation for Super-Resolution with Second-Order Degradation and Reconstruction ”

Contents

A More Details of the Second-Order Degradation

In our second-order degradation scheme, we randomly generate different degradations to degrade the test image into its second-order degraded counterparts. In this section, we illustrate how to randomly generate different types of degradations. Notably, we degrade the test images on the GPU device to accelerate the degradation process.

A.1 Random Blur Degradation

Following [26, 22], we model blur degradation as a convolution with a linear Gaussian blur filter/kernel. Given a test image, we randomly generate a set of isotropic or anisotropic Gaussian kernels $\mathbf{k}$ and use them to perform blur degradation on the test image. The probabilities of generating an isotropic kernel and an anisotropic kernel are set to 0.5 and 0.5, respectively. The size of each generated kernel is uniformly sampled from $\{7 \times 7, 9 \times 9, ..., 21 \times 21\}$. We sample the standard deviation of the blur kernel along the two principal axes σ_1 and σ_2 uniformly from $[0.2, 3]$. If $\mathbf{k}$ is an isotropic Gaussian blur kernel, we set σ_2 equal to σ_1. If $\mathbf{k}$ is an anisotropic Gaussian kernel, we further sample a rotation angle a uniformly from $[-\pi, \pi]$, and use a rotation matrix to transform the generated kernel based on the angle a. More details about how to generate a Gaussian blur kernel can refer to Real-ESRGAN [22].

A.2 Random Noise Degradation

In our second-order degradation, we randomly generate a set of Gaussian noise maps $\mathbf{n}$, and add them to the test image to obtain a set of second-order images with different additive Gaussian noise. With a probability of 60%, we generate noise for each channel of RGB images independently, otherwise, we generate the same noise map for all three channels. We first generate a noise map whose values are randomly generated from a normal Gaussian distribution. Then we sample a scale value to enlarge the noise uniformly from $[1, 30]$. More details can be referred to Real-ESRGAN [22].

A.3 Random JPEG Degradation

For JPEG compression $JPEG_q$, we sample a quality factor q uniformly from $[30, 95]$, and use the JPEG compression with the degradation q to degrade test images into a set of second-order degraded images with compression artifacts. Note that JPEG compression with a lower q compress the test image with a higher compression ratio and the compressed images are generally of a lower quality. To accelerate the degradation process, we use DiffJPEG[1], which is the PyTorch implementation of JPEG compression, to process the test image on the GPU device.

B The Difference from Real-ESRGAN

In this part, we would like to discuss the difference between our SRTTA with Real-ESRGAN[22], which proposes the concept of second-order degradations, to highlight the contribution of our SRTTA.

B.1 Solving Different Problems

Real-ESRGAN tries to enumerate all the degradations in real-world scenes and train an SR model to solve the image restoration on any degradation. However, it is non-trivial to obtain all real-world degradations, leading to domain shift issues when encountering unknown degradations during testing, as shown in Figure 11 of real-ESRGAN [22]. Unlike real-ESRGAN [22], our SRTTA aims to adapt the SR models to the test domains when test images contain unknown degradations. Our second-order degradation scheme aims to quickly construct the pseudo-paired data (instead of the paired training data) to adapt the SR model to the test domains.

B.2 Different Construction Schemes

Real-ESRGAN [22] proposes the second-order degradation to construct the paired training data, whose low-resolution (LR) images are obtained from the ground-truth high-resolution (HR) images.

[1]https://github.com/mlomnitz/DiffJPEG

Then, the paired data is used to train an SR model during the **training** phase in a **supervised** learning manner. Notably, the trained Real-ESRGAN [22] model is fixed during the test time. Instead, our second-order degradation scheme constructs the pseudo-paired data using the test images with unknown degradation (first-order degraded images). Our SRTTA model is continuously adapted to different domains during **testing** in a **self-supervised** learning manner.

C Experimental Datasets

C.1 Construction Details of the DIV2K-C Dataset

To evaluate the practicality, we construct a new benchmark dataset named DIV2K-C, which contains eight different degradations. We select the eight degradation types from the 15 corruptions of ImageNet-C [11] that do not extremely change the image content, including Gaussian Blur, Defocus Blur, Glass Blur, Gaussian Noise, Poisson Noise (Shot Noise), Impulse Noise, Speckle Noise, and JPEG compression. Unlike the ImageNet-C [11], we do not use the same degradation level to degrade all test images. Instead, we randomly generate the degradation level and further generate a degradation for each image based on the degradation level. Unlike prior SR methods that investigate a limited number of degradation types, the degradation scenarios we considered are more complex (eight degradation types in total), which is more practical for real-world applications.

Given a degradation, we use the classical image degradation model [17, 22] to generate the low-resolution (LR) test images from the high-resolution clean images. For blur degradation, we perform the blur convolution on the HR images and then use the Bicubic downsampling to obtain the test LR images. For noise and JPEG degradation, we first use the Bicubic downsampling to obtain clean LR images and then perform noise or JPEG degradation on the clean LR images to obtain the final test images. We show the visualization of some examples regarding each degradation type in Figure A.

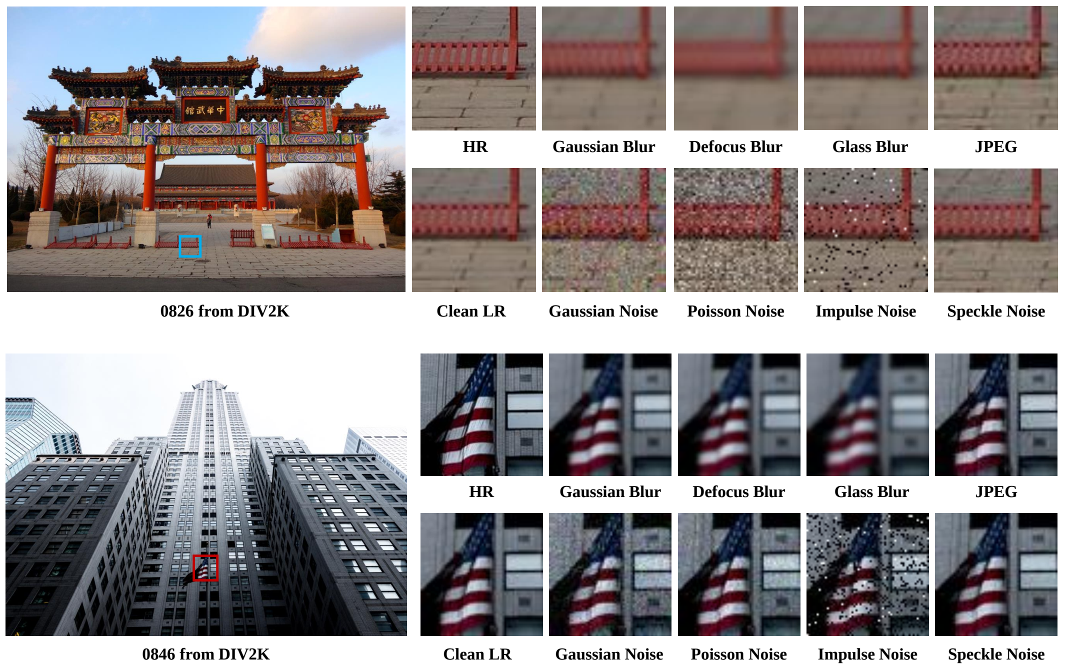

Figure A: The visualization of examples regarding each degradation type on the DIV2K-C dataset.

Gaussian blur. Following BSRGAN [26], we generate low-resolution (LR) images with Gaussian blur degradation. We randomly generate an isotropic Gaussian kernel or an anisotropic Gaussian kernel for each high-resolution (HR) image. Then, we use the blur kernel to perform blur convolution on the HR image and use Bicubic downsampling to obtain the final LR test images. For simplicity, we follow the recipe of BSRGAN [26] to generate test images with blur degradation.

Defocus blur. To better compare the performance of different SR methods, we also use the common Defocus blur degradation to degrade the HR images and obtain the LR images using the Bicubic downsampling. As illustrated in ImageNet-C [11], Defocus blur often occurs when an image is out of focus when we take pictures. We generate the blur kernel as ImageNet-C [11] and perform a blur convolution on the HR images. But unlike ImageNet-C [11], the degradation level of Defocus blur is randomly sampled from a given range.

Glass blur. We also choose another common degradation type, Glass Blur, which appears with "frosted glass" windows or panels [11]. This blur degradation requires two Gaussian blur operations and an operation that locally shuffles pixels between two blur operations. As mentioned above, the degradation level is randomly sampled from a given range, such as the standard deviation of the Gaussian blur kernel or the window size of the shuffling operation.

Gaussian noise. To generate test images with Gaussian noise, we sample the noise for each pixel from a normal Gaussian distribution. The mean of the Gaussian distribution is zero, and the standard deviation is uniformly sampled from the range of $\{2/255, 3/255, ..., 25/255\}$. More details can refer to the implementation of BSRGAN [26].

Poisson (Shot) noise. Poisson noise, also called Shot noise, can model the sensor noise caused by statistical quantum fluctuations. We randomly generate the Poisson noise map from a Poisson distribution, which has an intensity proportional to the image intensity. Then, we add the generated Poisson noise into the clean LR images to obtain the test images with Poisson noise. More details can refer to the implementation of Real-ESRGAN [22].

Impulse noise. Impulse noise is caused by errors in the data transmission generated in noisy sensors or communication channels, or by errors during the data capture from digital cameras [19]. The most common form of Impulse noise is called salt-and-pepper noise. To generate test images with Impulse noise, we uniformly select a set of pixels and replace them with zero or the maximum value (255). More details can be referred to ImageNet-C [11].

Speckle noise. Speckle noise is an additive noise where the noise added to a pixel tends to be larger if the original pixel intensity is larger. We first sampled the noise for each pixel from a Gaussian distribution and multiple the noise value by the original pixel. Last, we add the generated noise map into the LR clean images to obtain the final test images with Speckle noise.

JPEG compression. For JPEG compression, we use the OpenCV implementation of JPEG compression[2] to degrade the clean LR image into final test images. The compression quality factor q is randomly sampled from $[30, 90]$. We first encode the clean LR images into the bit stream using JPEG compression with the quality factor q and decode the bit stream to obtain the final test images. Note that JPEG compression is a lossy compression technique, so the final test images are inevitably corrupted with JPEG compression artifacts.

C.2 Construction Details of the DIV2K-MC Dataset

Since the real-world test images may contain multiple degradation types simultaneously, we further develop a new benchmark dataset named DIV2K-MC, which includes four test domains with mixed multiple degradations. The four domains are BlurNoise, BlurJPEG, NoiseJPEG and BlurNoiseJPEG. The test images in the BlurNoiseJPEG domain contain the combined degradation of Gaussian blur, Gaussian noise and JPEG degradations simultaneously.

BlurNoise. We generate LR images from HR images using Gaussian blur and Gaussian noise degradation. We first randomly generate a Gaussian blur kernel to perform blur convolution on the HR image. Then, we downsample the resulting image using Bicubic interpolation. Last, we randomly sample a Gaussian noise map and add it to the downsampled image to obtain the final LR image.

BlurJPEG. We generate LR images from HR images using Gaussian blur and JPEG degradation. We first randomly generate a Gaussian blur kernel to perform blur convolution on the HR image. Then, the resulting image is downsampled by using Bicubic interpolation. Last, we use JPEG compression with a random quality factor q to compress the downsampled image to obtain the final LR image.

NoiseJPEG. We generate LR images from HR images using Gaussian noise and JPEG degradation. We first downsample HR image using Bicubic interpolation. Then, we randomly sample a Gaussian

[2]https://github.com/opencv/opencv

noise map and add it to the downsampled image. Last, we use JPEG compression with a random quality factor q to compress the downsampled image to obtain the final LR image.

BlurNoiseJPEG. We generate LR images from HR images using Gaussian blur, Gaussian noise and JPEG degradation. We first randomly generate a Gaussian blur kernel to perform blur convolution on the HR image. Second, the resulting image is downsampled by using Bicubic interpolation. Then, we randomly sample a Gaussian noise map and add it to the downsampled image. Last, we use JPEG compression with a random quality factor q to compress the image to obtain the final LR image.

C.3 More Test Datasets for Test-Time Image Super-Resolution

Moreover, we also evaluate the performance of SR methods on real-world test images from DPED [13], ADE20K [28] and OST300 [23], whose corresponding ground-truth HR images can not be found. To evaluate the anti-forgetting performance, we report the adapted model performance on a clean benchmark dataset Set5 [2] whose images are clean images that are downsampled from HR images with Bicubic interpolation. Thus, these LR images do not contain any degradation.

D Implementation Details

D.1 Implementation Details of the Degradation Classifier

In our second-order degradation scheme, we use a pre-trained degradation classifier to predict the degradation type for each test image. To obtain the pre-trained degradation classifier, we use ResNet-50 [10] as the classifier and train it to recognize the degradation from test images.

In real-world scenes, test images may contain degradations other than these eight degradation types, such as ringing or overshoot artifacts [22], which may be viewed as variations of blur, noise or JPEG. Since it is infeasible to cover all the degradation types in real-world scenes, we make the degradation classifier to predict the coarse-level four classes, including clean, blur, noise and JPEG.

Training details. Specifically, we use the 800 training HR images of DIV2K and randomly crop them into patches with the size of 224 $\times$ 224 (instead of resizing them into 224 $\times$ 224). Similar to the construction of DIV2K-C, we degrade each patch using a random selection of one of eight degradation types. As for clean data, we do not perform any degradation on the patches. For training, we apply Adam with β_1 = 0.9, β_2 = 0.999 and set the batch size as 256. The learning rate is initialized to 10^{-3} and decreased to 10^{-6} with a cosine annealing out of 400 epochs in total.

Testing details. During testing, we directly input the whole test image **with original resolution** into the classifier and output the predicted results to recognize the degradation type. The predicted results of the multi-label degradation classifier $C(\cdot)$ are the probabilities of the three degradations, including blur, noise and JPEG degradation. If the predicted probability of one degradation type is larger than the threshold of 0.5, the test image is considered to contain the degradation of this type. The clean image means that this image does not contain any degradation such as blur, noise, or JPEG, and we directly use the pre-trained SR model to super-resolve these clean test images.

D.2 More Details of Super-Resolution Test-Time Adaptation

We use the baseline model of EDSR [16] with less than 2M parameters as our pre-trained SR model for 2$\times$ and 4$\times$ SR. During adaptation, we only update the parameters in the Resblock of the EDSR model. To avoid anti-forgetting, we use five clean test LR images from Set5 [2] to select important parameters to be frozen in Eqn. (9). Moreover, when evaluating the anti-performance Set5 [2], we directly use the adapted model to super-resolve the test images without using the classifier.

In our experiment, we conduct experiments in **parameter-reset** and **lifelong** settings. In the parameter-reset setting, the model parameters will be reset after the adaptation on each domain, which is the default setting of our SRTTA. In the lifelong setting, the model parameters will never be reset in the long-term adaptation, in this case, we call our methods as SRTTA-lifelong.

For test-time adaptation, we use the Adam optimizer with the learning rate of 5×10^{-5} for the pre-trained SR models. We set the batch size N to 32, and we randomly crop the test image into N patches of size 96×96 and 64×64 for 2$\times$ and 4$\times$ SR, and degrade them into second-order degraded patches. We perform $S = 10$ iterations of adaptation for each test image. For the balance weight in

Eqn. (6), we set α to 1. For the ratio of parameters to be frozen, we set the ρ to 0.50. To compare the inference times of different SR methods, we measure all methods on a TITAN XP with 12G graphics memory for a fair comparison. Due to the memory overload of HAT [6] and DDNM [24], we chop the whole image into smaller patches and process them individually for these two methods. In our experiments, we use the bold number to indicate the best result and the underlined number to indicate the second-best result.

E More Experimental Results

E.1 More Results of Test-Time Image Super-Resolution

In this part, we compare our SRTTA with existing SR methods, including supervised pre-trained SR methods, blind SR methods, zero-shot SR methods, and a TTA baseline with consistency loss. 1) The supervised pre-trained SR methods learn to process test images with a predefined degradation process, i.e., the Bicubic downsampling. These methods include the EDSR baseline [16], SwinIR [15], IPT [5] and HAT [6], SRDiff [14], and Real-ESRNet [22]. Note that Real-ESRNet [22] is the PSNR-oriented model of Real-ESRGAN [22], which use a complex combination of different degradation to construct pair training data, including Gaussian blur, Gaussian Noise, Poisson Noise and JPEG compression, and so on. 2) Blind SR models predict the blur kernel of test images and generate HR images simultaneously, we compare with the state-of-the-art DAN [12] and DCLS-SR [18] methods. 3) Zero-shot SR models construct the LR-HR paired images based on the assumption of the cross-scale patch recurrence and train/update their SR model for each test image. These methods include ZSSR [20], KernelGAN [1]+ZSSR [20], MZSR [7], DualSR [8], DDNM [24]. 4) Moreover, we implement a baseline TTA method (dubbed TTA-C) that utilizes the augmentation consistency loss in Eqn. (8) to adapt the pre-trained model, similar to MEMO [27] and CoTTA [21].

We provide more results of our SRTTA for 2$\times$ and 4$\times$ SR in terms of PSNR and SSIM metrics. As shown in Table A and Table B, our SRTTA consistently outperforms existing SR methods on the DIV2K-C dataset on average. We further provide more visualization results in Figure D, E, F and G, which demonstrate our SRTTA is able to remove the degradation from test images and generate plausible HR images. These results demonstrate that our SRTTA is able to quickly adapt the pre-trained SR model to the test images with different degradation.

Table A: We report the PSNR/SSIM results of all corruption fields in DIV2K-C for 2$\times$ SR.

Methods	GaussianBlur	DefocusBlur	GlassBlur	GaussianNoise	PossionNoise	ImpulseNoise	SpeckleNoise	JPEG	Mean	GPU Time
	PSNR/SSIM	PSNR/SSIM	PSNR/SSIM	PSNR/SSIM	PSNR/SSIM	PSNR/SSIM	PSNR/SSIM	PSNR/SSIM	PSNR/SSIM	(seconds/image)
Bicubic	28.04/0.803	24.10/**0.784**	26.31/0.745	25.35/0.554	23.33/0.496	15.28/0.324	28.65/0.774	28.28/0.806	24.92/0.661	-
SwinIR [15]	30.40/0.838	25.52/0.673	27.82/0.773	25.35/0.510	22.36/0.428	15.34/0.242	30.45/0.774	30.74/0.846	26.00/0.636	13.08
IPT [5]	28.93/0.820	24.08/0.640	26.39/0.749	22.96/0.439	20.08/0.369	13.06/0.241	28.27/0.728	28.36/0.804	24.02/0.599	55.36
HAT [6]	29.00/0.821	24.08/0.640	26.40/0.749	22.31/0.417	19.33/0.349	11.91/0.192	28.02/0.722	28.25/0.802	23.66/0.587	25.01
DAN [12]	**34.32/0.916**	25.58/0.673	31.77/0.872	26.36/0.558	23.28/0.461	11.46/0.203	30.64/0.777	31.08/0.857	26.81/0.665	3.10
DCLS-SR [18]	33.93/0.914	25.55/0.671	**31.98/0.872**	25.45/0.521	21.59/0.415	8.12/0.112	30.66/0.784	30.86/0.848	26.02/0.642	1.45
ZSSR [20]	29.91/0.831	25.54/0.674	27.79/0.771	26.79/0.590	24.24/0.509	**19.14/0.375**	30.95/0.813	31.01/0.853	26.92/0.677	117.65
KernalGAN [1]+ZSSR	30.18/0.859	**25.87**/0.679	29.01/0.808	21.45/0.436	19.32/0.366	17.93/0.354	25.07/0.686	26.11/0.774	24.37/0.620	231.41
MZSR [7]	30.14/0.838	25.54/0.670	28.03/0.777	25.94/0.543	23.48/0.472	17.05/0.314	30.00/0.771	30.49/0.845	26.33/0.654	3.34
DualSR [8]	29.00/0.854	24.40/0.640	28.18/0.805	22.30/0.509	20.11/0.436	17.22/0.376	24.99/0.738	24.74/0.751	23.87/0.639	210.85
DDNM [24]	28.46/0.808	24.09/0.636	26.39/0.744	24.37/0.497	21.92/0.432	13.98/0.310	28.60/0.753	28.26/0.802	24.51/0.623	2,288.55
EDSR [16]	30.28/0.837	25.52/0.673	27.82/0.773	25.87/0.536	22.96/0.449	15.87/0.269	30.52/0.778	30.83/0.847	26.21/0.645	-
TTA-C	30.21/0.835	25.50/0.673	27.79/0.772	26.37/0.559	23.57/0.473	16.40/0.298	30.25/0.783	30.91/0.849	26.38/0.655	13.59
SRTTA (ours)	31.07/0.869	25.86/0.674	29.01/0.815	**29.65**/0.762	26.69/0.637	16.15/0.284	**32.33/0.873**	**31.30/0.857**	**27.76**/0.721	5.38
SRTTA-lifelong (ours)	31.07/0.869	25.83/0.674	29.18/0.819	29.48/**0.797**	**27.10/0.673**	16.27/0.273	31.71/0.864	31.22/0.853	27.73/**0.728**	5.38

Table B: We report the PSNR/SSIM results of all corruption fields in DIV2K-C for 4$\times$ SR.

Methods	GaussianBlur	DefocusBlur	GlassBlur	GaussianNoise	PossionNoise	ImpulseNoise	SpeckleNoise	JPEG	Mean	GPU Time
	PSNR/SSIM	PSNR/SSIM	PSNR/SSIM	PSNR/SSIM	PSNR/SSIM	PSNR/SSIM	PSNR/SSIM	PSNR/SSIM	PSNR/SSIM	(seconds/image)
Bicubic	25.83/0.718	24.10/0.641	25.35/0.699	23.17/0.500	22.15/0.475	15.1/0.384	25.29/0.658	25.07/0.681	23.27/0.595	-
Real-ESRNet [22]	26.82/0.765	25.17/0.704	26.75/0.762	25.49/**0.701**	25.06/**0.692**	**19.24/0.509**	26.47/0.749	25.70/0.720	25.09/**0.700**	1.12
SwinIR [15]	28.48/0.785	25.81/0.692	27.44/0.753	22.96/0.454	21.40/0.420	14.59/0.225	26.66/0.670	27.25/0.731	24.32/0.591	8.15
IPT [5]	26.98/0.760	24.36/0.660	25.98/0.726	20.94/0.385	19.30/0.357	12.86/0.270	24.89/0.628	25.22/0.685	22.57/0.559	35.29
HAT [6]	27.09/0.764	24.37/0.660	26.01/0.728	20.38/0.368	18.76/0.344	11.65/0.177	24.70/0.623	25.11/0.680	22.26/0.543	5.95
DAN [12]	28.71/0.809	25.02/0.679	28.88/0.812	21.79/0.414	20.26/0.387	8.70/0.110	25.10/0.631	25.21/0.686	22.96/0.566	1.18
DCLS-SR [18]	**30.38/0.834**	**26.48/0.709**	**30.58/0.838**	24.43/0.525	22.90/0.479	6.94/0.038	27.27/0.696	27.46/0.736	24.56/0.607	1.47
ZSSR [20]	27.84/0.763	25.83/0.691	27.34/0.745	24.26/0.543	23.04/0.500	17.75/0.402	26.72/0.700	27.03/0.727	24.97/0.634	117.34
KernalGAN [1]+ZSSR	26.04/0.754	25.84/0.696	26.75/0.755	20.64/0.427	19.63/0.407	16.58/0.361	22.50/0.578	23.36/0.663	22.67/0.580	417.80
MZSR [7]	25.76/0.722	25.05/0.676	25.77/0.712	22.38/0.471	21.37/0.429	16.46/0.342	24.20/0.621	25.09/0.695	23.26/0.584	2.14
SRDiff [14]	26.52/0.746	24.18/0.649	25.92/0.723	16.25/0.180	15.50/0.172	12.23/0.172	19.41/0.356	24.18/0.649	20.52/0.456	72.22
EDSR [16]	28.31/0.780	25.81/0.692	27.40/0.751	23.49/0.479	22.10/0.443	15.28/0.283	26.80/0.676	27.34/0.734	24.57/0.605	-
TTA-C	28.19/0.776	25.76/0.691	27.29/0.747	24.03/0.504	22.71/0.468	16.38/0.357	27.03/0.685	27.45/0.736	24.85/0.621	20.11
SRTTA (ours)	28.61/0.792	26.24/0.702	28.09/0.775	**26.58**/0.684	25.27/0.617	15.73/0.318	**28.24/0.763**	**27.66/0.742**	**25.80**/0.674	4.47
SRTTA-lifelong (ours)	28.61/0.792	26.25/0.701	28.18/0.776	26.43/0.699	**25.56**/0.658	15.92/0.312	27.74/0.757	27.61/0.740	25.79/0.679	4.47

E.2 More Results on Test domains with Mixed Multiple Degradations.

In this part, we evaluate our SRTTA on DIV2K-MC, which consists of four test domains with mixed multiple degradations. In Table C, our SRTTA achieves the best performance on 4 domains with different mixed degradations, e.g., 0.619 (DualSR) $\rightarrow$ 0.775 (our SRTTA-lifelong) regarding the average SSIM metric. These results further validate the effectiveness of our proposed methods.

Table C: Comparison results with prior methods on DIV2K-MC. We report the PSNR(↑)/SSIM(↑) values of different methods.

Methods	BlurNoise	BlurJPEG	NoiseJPEG	BlurNoiseJPEG	Mean
SwinIR [15]	20.91/0.311	26.83/0.748	23.86/0.523	22.77/0.450	23.59/0.508
IPT [5]	21.28/0.327	26.83/0.748	24.15/0.535	22.96/0.459	23.81/0.517
HAT [6]	23.41/0.399	28.86/0.788	25.69/0.572	24.42/0.502	25.59/0.565
DAN [12]	24.14/0.438	28.95/0.791	26.20/0.593	24.82/0.519	26.03/0.585
DCLS-SR [18]	23.84/0.420	28.93/0.790	26.37/0.599	24.92/0.523	26.02/0.583
ZSSR [20]	24.95/0.493	29.02/0.793	26.68/0.617	25.24/0.542	26.47/0.611
KernelGAN [1]+ZSSR	23.08/0.424	28.32/0.786	21.90/0.474	22.76/0.443	24.02/0.532
MZSR [7]	18.73/0.213	24.90/0.667	20.37/0.398	20.62/0.354	21.16/0.408
DualSR [8]	25.59/0.561	28.24/0.787	23.78/0.586	24.62/0.541	25.56/0.619
DDNM [24]	22.62/0.389	26.82/0.746	25.11/0.582	23.81/0.504	24.59/0.555
EDSR [16]	24.02/0.430	28.93/0.790	26.08/0.587	24.73/0.514	25.94/0.580
TTA-C	24.29/0.446	28.93/0.790	26.35/0.598	24.91/0.522	26.12/0.589
SRTTA (ours)	26.93/0.709	28.93/**0.798**	**29.13/0.784**	27.12/0.728	28.02/0.755
SRTTA-lifelong (ours)	**27.67/0.749**	**29.02**/0.793	29.70/0.810	**27.52/0.747**	**28.48/0.775**

E.3 More Results of Ablation Studies

Effect of each component. In this part, we investigate the effect of each component and provide more ablation studies. As shown in Table D, the baseline without the degradation classifier, generates the second-order degraded images with random degradation types, achieving a limited performance in terms of both PSNR and SSIM. The baseline without the adaptation consistency loss $\mathcal{L}_a$ results in the model collapse due to the lack of the consistency constraint. Without the self-supervised adaptation loss $\mathcal{L}_s$, the TTA performance of the adapted model drops significantly. These experimental results demonstrate the effectiveness of each component of our framework.

Table D: We report the PSNR/SSIM results of ablation studies of different components for 2$\times$ SR.

Methods	GaussianBlur	DefocusBlur	GlassBlur	GaussianNoise	PossionNoise	ImpulseNoise	SpeckleNoise	JPEG	Mean
	PSNR/SSIM	PSNR/SSIM	PSNR/SSIM	PSNR/SSIM	PSNR/SSIM	PSNR/SSIM	PSNR/SSIM	PSNR/SSIM	PSNR/SSIM
SRTTA (ours)	**31.07/0.869**	25.86/0.674	**29.01/0.815**	**29.66/0.762**	**26.69/0.637**	**16.15/0.284**	**32.33/0.873**	**31.30/0.857**	**27.76/0.721**
- w/o classifier $C(\cdot)$	29.43/0.812	25.51/0.675	27.51/0.756	22.05/0.546	25.64/0.571	15.66/0.260	31.50/0.836	31.19/0.855	26.06/0.664
- w/o $\mathcal{L}_s$	30.65/0.854	**25.87/0.680**	28.43/0.795	28.04/0.644	24.83/0.534	15.96/0.274	31.96/0.847	31.47/0.862	27.15/0.686
- w/o $\mathcal{L}_a$	12.29/0.254	5.67/0.397	5.65/0.403	12.87/0.477	10.29/0.072	11.48/0.213	11.67/0.218	11.99/0.477	10.24/0.314

Effect of the hyperparameter α in Eqn. (6). In this part, we investigate the effect of the weight of adaptation consistency loss α. As shown in Table E, the adapted model with $\alpha = 1$ achieves the best TTA performance. Thus, we set the $\alpha = 1$ by default for our SRTTA during adaptation.

Table E: We report the PSNR/SSIM results of ablation studies of α for 2$\times$ SR.

α	GaussianBlur	DefocusBlur	GlassBlur	GaussianNoise	PossionNoise	ImpulseNoise	SpeckleNoise	JPEG	Mean	Set5
	PSNR/SSIM	PSNR/SSIM	PSNR/SSIM	PSNR/SSIM	PSNR/SSIM	PSNR/SSIM	PSNR/SSIM	PSNR/SSIM	PSNR/SSIM	PSNR/SSIM
0	12.29/0.254	5.67/0.397	5.65/0.403	12.87/0.477	10.29/0.072	11.48/0.213	11.67/0.218	11.99/0.477	10.24/0.314	11.42/0.421
0.1	11.11/0.318	8.02/0.043	5.65/0.403	22.78/0.683	5.65/0.403	12.50/0.484	15.03/0.542	30.95/0.850	13.96/0.466	37.66/0.959
0.5	10.47/0.134	10.46/0.313	23.69/0.708	29.21/**0.797**	**27.80/0.717**	**16.30/0.290**	32.10/0.871	30.98/0.850	22.63/0.585	**37.75/0.959**
1	**31.07/0.869**	25.86/0.674	**29.01/0.815**	**29.66**/0.762	26.69/0.637	16.15/0.284	**32.33/0.873**	**31.30/0.857**	**27.76/0.721**	34.59/0.924
2	30.86/0.862	25.91/0.678	28.71/0.804	29.04/0.710	25.89/0.591	16.06/0.279	32.23/0.865	31.45/0.861	27.52/0.706	35.41/0.933
5	30.74/0.857	**25.91/0.680**	28.53/0.798	28.47/0.670	25.29/0.558	16.00/0.276	32.08/0.855	31.48/0.862	27.31/0.695	35.89/0.939

Effect of the hyperparameter ρ in Eqn. (9). In this part, we analyze the effect of the hyperparameter ρ, which decides the ratio of parameters to freeze, for the test-time adaptation. In Table F, when $\rho = 0.50$, our SRTTA achieves the best TTA performance on the DIV2K-C dataset on average in the lifelong setting. Meanwhile, we also investigate the effect of the adaptive parameter preservation (APP) strategy in the parameter-reset setting. As shown in Table F, our APP strategy (with $\rho = 0.50$)

merely has little impact on the TTA in the parameter-reset setting. These results demonstrate the effectiveness of the APP strategy in test-time adaptation for image super-resolution.

Table F: We report the PSNR/SSIM results of ablation studies of ρ for $2\times$ SR in the parameter-reset and lifelong setting, our model is SRTTA and SRTTA-lifelong.

Setting	0	0.1	0.2	0.3	0.5	0.7	0.9	1
SRTTA	27.74/0.729	27.79/0.730	**27.82/0.729**	27.82/0.727	27.76/0.721	27.55/0.709	27.08/0.682	26.21/0.645
SRTTA-lifelong	27.46/0.726	27.60/0.727	27.66/0.728	27.72/0.728	**27.73/0.728**	27.73/0.725	27.50/0.706	26.21/0.645

Comparison with other anti-forgetting methods. In this part, we compare our adaptive parameter preservation (APP) strategy with two baseline methods to demonstrate the effectiveness of our strategy in preserving the learned knowledge of pre-trained SR models. **Stochastic Restoration (STO)** [21] randomly selects a different set of parameters (with a ratio of 1%) and restores them back to the parameters of the pre-trained models. **Random Selection (RS)** selects a fixed set of parameters before adaption and freezes them not to update. As shown in Table G, our APP strategy achieves the best TTA results on the DIV2K-C dataset. Meanwhile, with the same ratio of selected parameters, our APP strategy consistently outperforms the Random Selection baseline for the anti-forgetting. These results demonstrate that our adaptive selection is able to select the important parameters and preserve the knowledge of the pre-trained model.

Table G: We report the PSNR/SSIM results of ablation studies of adaptive parameter preservation (APP) strategy for $2\times$ SR in the lifelong setting.

Dataset	STO [21]	RS with different ρ			APP with different ρ (ours)		
		0.3	0.5	0.7	0.3	0.5	0.7
DIV2K-C (with degradation shift)	27.17/0.687	27.52/0.727	27.62/0.728	27.68/0.726	27.72/0.728	**27.73/0.728**	27.73/0.725
Set5 (w/o degradation shift)	**35.57/0.938**	33.95/0.913	34.02/0.914	34.24/0.918	34.11/0.916	34.23/0.917	34.38/0.920

E.4 Effectiveness on a New Unknown Domain

In this part, we further evaluate our SRTTA on a new unknown domain with the degradation of processed camera sensor noise [3, 26], which is not used in the training phase of the SR model or that of the degradation classifier. We report the PSNR(↑) and SSIM(↑) values of different methods on 100 images with random processed camera sensor noise. In Table H, our SRTTA method is also able to improve the model performance on this unknown degradation. These experimental results further demonstrate the generalization capability of our SRTTA model to unknown degradation types.

E.5 Comparison with Patch-Recurrence Reconstruction Loss

In this part, we investigate the effect of our second-order reconstruction loss. We compare our loss with the loss of existing zero-shot methods [20, 7, 1]. Based on the assumption of patch recurrence across scales [9, 29], these methods downsample the test image to obtain an image with a lower resolution and reconstruct the test image from the downsampled image. For simplicity, we call this patch-recurrence loss. For a fair comparison, we further downsample the second-order degraded images that are obtained using our second-order degradation scheme and reconstruct the test image with the patch-recurrence loss. As shown in Table I, our SRTTA with our second-order reconstruction loss consistently outperforms the baseline with the patch-recurrence loss. These results demonstrate the effectiveness of our second-order reconstruction loss.

Table H: Results of different methods on the unknown domain with the degradation of processed camera sensor noise.

Methods	PSNR	SSIM
SwinIR [15]	19.45	0.496
IPT [5]	19.51	0.500
HAT [6]	21.52	0.596
DDNM [24]	19.63	0.518
DAN [12]	21.53	0.598
DCLS-SR [18]	21.57	0.605
DualSR [8]	21.14	0.586
MZSR [7]	20.40	0.438
ZSSR [20]	21.57	0.621
KernelGAN [1]+ZSSR	20.60	0.543
EDSR [16]	21.56	0.601
SRTTA (ours)	**21.81**	**0.647**

E.6 Effect of the Feature-level Reconstruction

In this part, we investigate the effect of different reconstruction levels. In our second-order reconstruction, we use the feature-level reconstruction to adapt the pre-trained model as in Eqn. (6). We

Table I: We report the PSNR/SSIM results of ablation studies of the patch-recurrence reconstruction loss for 2×SR in parameter-reset and lifelong settings.

methods	Setting	GaussianBlur	DefocusBlur	GlassBlur	GaussianNoise	PossionNoise	ImpulseNoise	SpeckleNoise	JPEG	Mean
		PSNR/SSIM	PSNR/SSIM	PSNR/SSIM	PSNR/SSIM	PSNR/SSIM	PSNR/SSIM	PSNR/SSIM	PSNR/SSIM	PSNR/SSIM
Patch-recurrence loss	parameter-reset	29.87/0.828	25.51/0.674	27.67/0.767	28.55/0.680	26.41/0.605	19.72/0.407	31.71/0.842	31.02/0.853	27.56/0.707
Patch-recurrence loss	lifelong	29.87/0.828	25.51/0.674	27.67/0.767	28.52/0.678	26.40/0.604	**20.48/0.430**	31.76/0.846	31.01/0.853	27.65/0.710
SRTTA(ours)	parameter-reset	31.07/0.869	**25.86**/0.674	29.01/0.815	**29.66**/0.762	26.69/0.637	16.15/0.284	**32.33/0.873**	**31.30/0.857**	**27.76**/0.721
SRTTA(ours)	lifelong	**31.07/0.869**	25.83/**0.674**	**29.18/0.819**	29.48/**0.797**	**27.10/0.673**	16.27/0.273	31.71/0.864	31.22/0.853	27.73/**0.728**

Table J: We report the PSNR/SSIM results of ablation studies of feature-level and image-level reconstruction for 2× SR in the lifelong setting.

Reconstruct-level	Scale	GaussianBlur	DefocusBlur	GlassBlur	GaussianNoise	PossionNoise	ImpulseNoise	SpeckleNoise	JPEG	Mean
		PSNR/SSIM	PSNR/SSIM	PSNR/SSIM	PSNR/SSIM	PSNR/SSIM	PSNR/SSIM	PSNR/SSIM	PSNR/SSIM	PSNR/SSIM
EDSR [16]	2	30.28/0.837	25.52/0.673	27.82/0.773	25.87/0.536	22.96/0.449	15.87/0.269	30.52/0.778	30.83/0.847	26.21/0.645
Image-level	2	**31.21/0.871**	25.73/0.671	29.16/0.817	**29.56**/0.796	26.74/0.654	16.24/0.263	**32.47/0.884**	**31.44/0.860**	**27.82**/0.727
Feature-level	2	31.07/0.869	**25.83/0.674**	**29.18/0.819**	29.48/**0.797**	**27.10/0.673**	**16.27/0.273**	31.71/0.864	31.22/0.853	27.73/**0.728**
EDSR [16]	4	28.31/0.780	25.81/0.692	27.40/0.751	23.49/0.479	22.10/0.443	15.28/0.283	26.80/0.676	27.34/0.734	24.57/0.605
Image-level	4	28.61/0.790	26.23/0.697	28.13/0.773	26.46/0.685	25.28/0.623	**15.72/0.297**	**28.02**/0.751	**27.74/0.746**	**25.77**/0.670
Feature-level	4	**28.78/0.795**	**26.31/0.703**	**28.16/0.776**	**26.28/0.691**	**25.46/0.643**	15.62/0.294	27.77/**0.755**	27.61/0.740	25.75/**0.675**

compare a baseline with an image-level reconstruction, which means we reconstruct the output of the SR model instead of the feature in the middle layer. As shown in Table J, when reconstructing at the image level, the adapted model achieves a comparable performance for both 2× SR and 4× SR. Thus, both reconstruction levels are optional, we use the feature-level reconstruction by default.

Table K: We report the PSNR/SSIM results of ablation studies of adapted iterations for 2× SR in the parameter-reset setting.

Iterations	GaussianBlur	DefocusBlur	GlassBlur	GaussianNoise	PossionNoise	ImpulseNoise	SpeckleNoise	JPEG	Mean	GPU Time
	PSNR/SSIM	PSNR/SSIM	PSNR/SSIM	PSNR/SSIM	PSNR/SSIM	PSNR/SSIM	PSNR/SSIM	PSNR/SSIM	PSNR/SSIM	seconds/image
1	30.49/0.844	25.59/0.675	28.08/0.782	27.05/0.592	24.34/0.507	15.98/0.279	31.32/0.810	31.09/0.853	26.74/0.668	0.60
2	30.72/0.854	25.82/**0.679**	28.62/0.800	27.76/0.630	24.99/0.538	16.02/0.280	31.76/0.830	31.23/0.856	27.12/0.683	1.41
5	30.64/0.861	25.80/0.677	28.88/0.811	28.90/0.702	26.10/0.600	15.98/0.278	32.19/0.861	**31.37/0.859**	27.48/0.706	2.73
10	31.07/**0.869**	**25.86**/0.674	29.01/0.815	**29.66**/0.762	**26.69/0.637**	**16.15/0.284**	**32.33/0.873**	31.30/0.857	**27.76/0.721**	5.38
20	**31.15**/0.870	25.80/0.675	**29.32/0.824**	29.24/**0.772**	26.05/0.601	16.08/0.276	32.14/0.865	31.31/0.856	27.64/0.717	10.82
50	30.71/0.856	25.64/0.674	29.28/0.821	29.12/0.743	25.40/0.569	16.02/0.265	31.54/0.838	28.46/0.846	27.02/0.701	25.64

E.7 Effect of Adaptation Iterations for Each Image

In this part, we investigate the effect of different adaptation iterations for each image. As shown in Table K, we compare the TTA performance of SRTTA with a different number of iterations S for each image. When the number of iterations S is small, the adapted SR model is not able to learn how to remove the degradation for these images well. When the number of iterations S is too large, the performance improvement of SRTTA diminishes and the adaptation cost will be greatly increased. Thus, we set S to 10 for a better efficiency-accuracy trade-off.

E.8 The Statistics of the Degradation Types of Real-world Images

In this part, we count the statistics of the degradation types of real-world images and report the results in Table L. We use our degradation classifier to identify the degradation types of real-world images from five datasets, including RealSR [4], DRealSR [25], DPED [13], OST300 [23] and ADE20K [28]. Experimental results in Table L show that the degradation type of blur happens the most among these real-world datasets.

E.9 Further Analysis of the Domain Shift Issue

In this part, we investigate the effect of the domain shift issues for pre-trained SR models, which are trained on specific domains with different degradation types. We use the EDSR baseline model as the model for analysis. In total, we separately train four EDSR baseline models on clean, blur, noise and JPEG domains, respectively. The corresponding four models are named EDSR, EDSR-B, EDSR-N and EDSR-J, respectively. We evaluate these four models on clean images and the test images with Gaussian Blur, Gaussian Noise or JPEG degradations in Figure B and Figure C.

As shown in Figure B and Figure C, when domain shift occurs, the pre-trained EDSR models, which are trained on domains different from the test domains, cannot remove the degradation from test

Table L: The count of the predicted degradation types of the real-world images from the five datasets. Note that some images can contain more than one degradation type simultaneously.

Dataset (# Images)	Clean	Blur	Noise	JPEG
RealSR (912)	48	860	1	149
DRealSR (35148)	1378	33770	0	1
DPED (187)	103	33	21	64
OST300 (300)	52	23	14	221
ADE20K (27574)	0	3452	2424	27573
Total (64121)	1581	**38138**	2460	28008

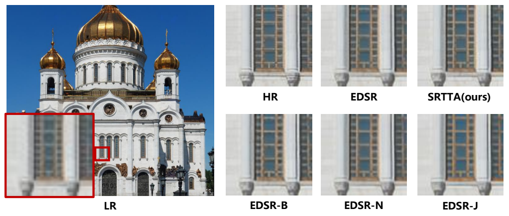

(a) Visualization results under clean domain.

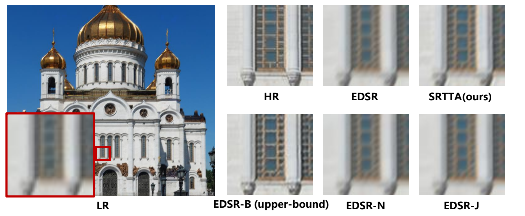

(b) Visualization results under Gaussian Blur.

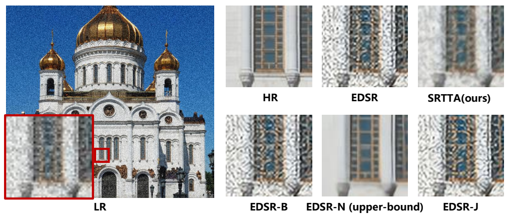

(c) Visualization results under Gaussian Noise.

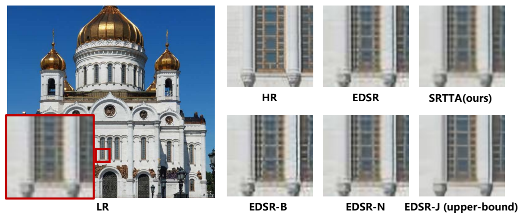

(d) Visualization results under JPEG.

Figure B: Visualization of the domain shift issue under different domains for $2\times$ SR.

images and generate unsatisfactory HR images with artifacts. For example, EDSR-B models cannot remove the noise and JPEG degradation, the EDSR-N and EDSR-J are also unable to remove the blur degradation. Instead, after test-time adaptation, our SRTTA is capable of handling the test images with unknown degradations and generating HR images with fewer artifacts. For example, our SRTTA is able to generate sharper HR images than EDSR-N and EDSR-J under Gaussian Blur domains. Indeed, our SRTTA models may be unable to completely remove the degradation compared with the upper-bound models, such as EDSR-B under Gaussian Blur. Thus, these drawbacks are required to be further addressed in future works.

F Visualization Results

F.1 Visualization Results on the DIV2K-C Images

In this part, we show more visualization comparison results of different SR methods on test images of the DIV2K-C dataset for both $2\times$ and $4\times$ SR. As shown in Figures D and E, our SRTTA is able to reduce the degradation from the test images and generate more plausible HR images.

F.2 Visualization Results on the Real-World Images

In this part, we conduct a comprehensive comparison of our SRTTA with existing approaches on two real-world datasets, including DPED [13], ADE20K [28] and OST300 [23]. As shown in Figures F and G, our SRTTA methods consistently generate more satisfactory HR images with less degradation of unknown noise or artifacts.

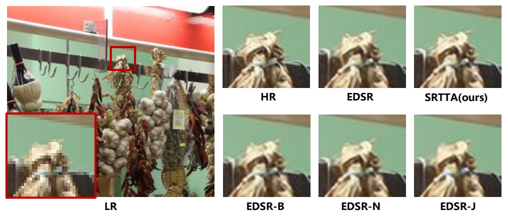

(a) Visualization results under clean domain.

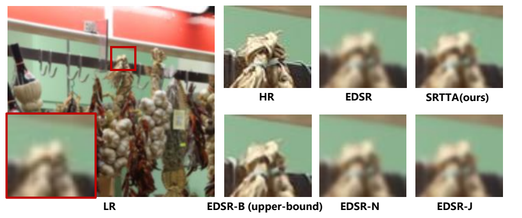

(b) Visualization results under Gaussian Blur.

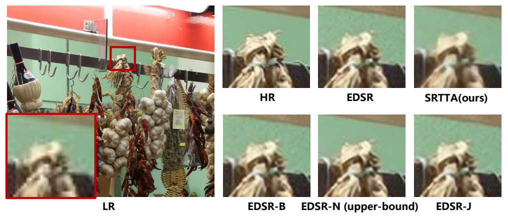

(c) Visualization results under Gaussian Noise.

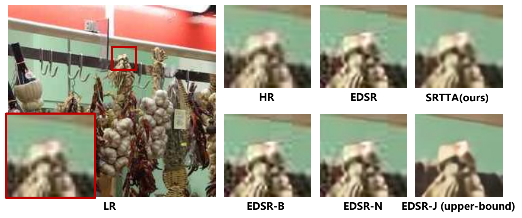

(d) Visualization results under JPEG.

Figure C: Visualization of the domain shift issue under different domains for 2× SR.

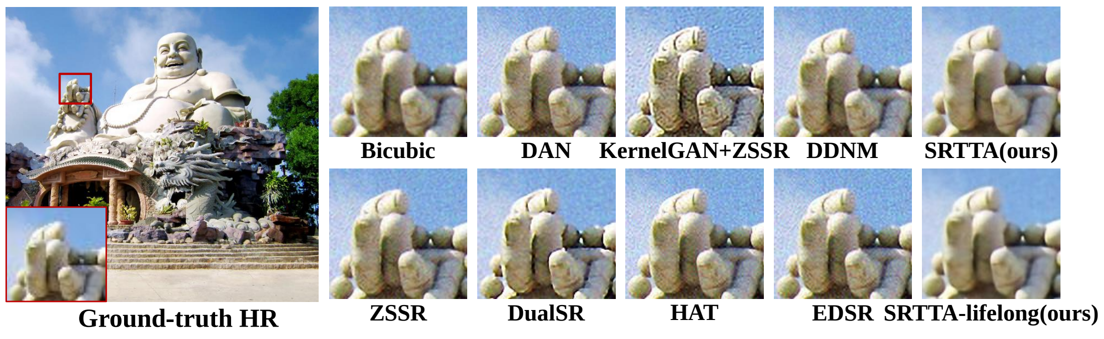

(a) Visualizations under Gaussian Noise for 2× SR

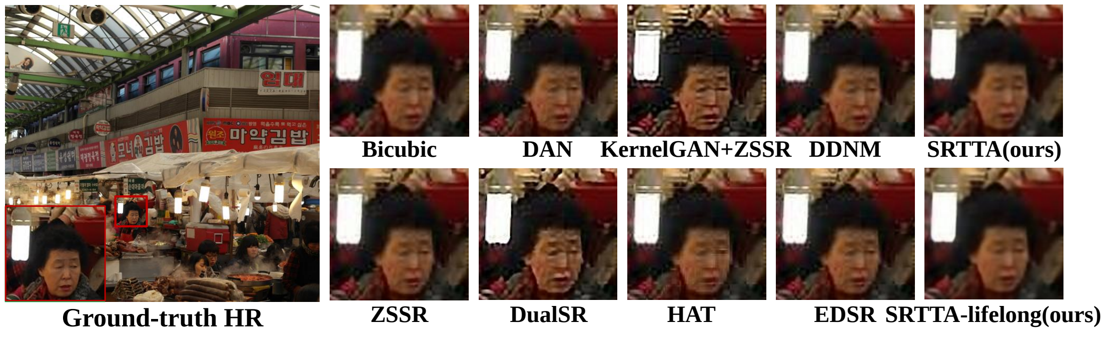

(b) Visualizations under JEPG Compression for 2× SR

Figure D: Visualization comparison on DIV2K-C test images with degradation for 2× SR.

G Limitation Analysis and Border Impacts

G.1 Limitation Analysis

In this part, we analyze the limitations of our SRTTA and existing SR methods. When test images are corrupted at a high level, our SRTTA may not be able to completely remove the degradation and result in generated HR images with the existing degradation. For example, we show more visualization results of different methods on test images with Impulse Noise degradation in Figure H.

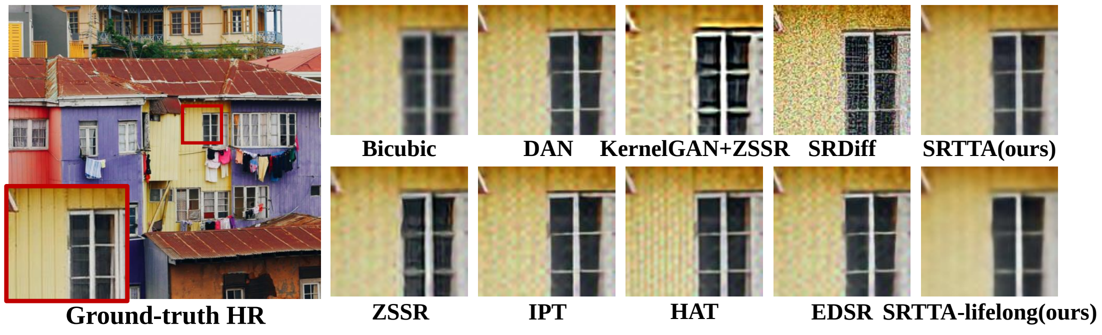

(a) Visualizations under PossionNoise for 4× SR

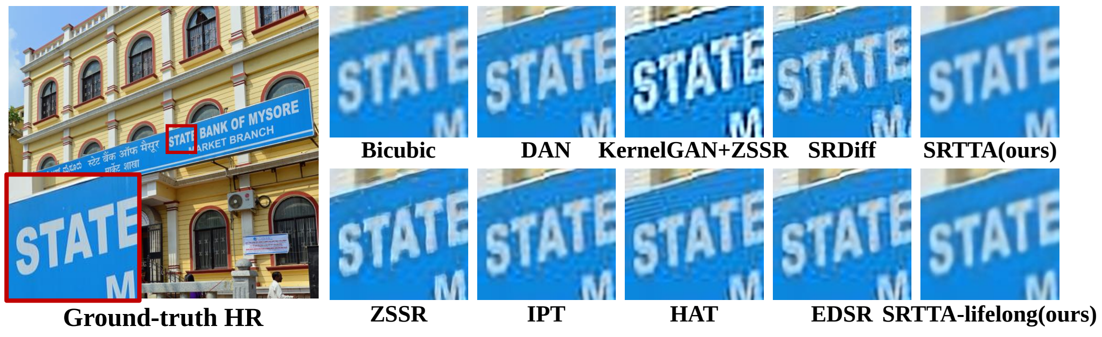

(b) Visualizations under JEPG Compression for 4× SR

Figure E: Visualization comparison on DIV2K-C test images with degradation for 4× SR.

Since Real-ESRGAN [22] uses several different degradation types to construct training data, this model is able to remove the degradation in many cases. However, this model still suffers from the degradation shift issue, such as it cannot remove the gray Impulse noise from the test images as shown in Figure H(a). Moreover, Real-ESRGAN may generate HR images with over-smooth regions when removing the noise degradation and introduce some unpleasant artifacts due to the GAN training [22], which are shown in Figure H(b) and Figure H(c), respectively. Although our SRTTA cannot also completely remove the degradation from the test images in these cases, our SRTTA often preserves the original information of the test images. These results show the limitations of our SRTTA and existing methods and have a great impact on the practical application. Thus, these drawbacks are in urgent need to address in future works.

G.2 Broader Impacts

Our proposed SRTTA method is capable of improving the resolution of low-resolution test images in real-world applications, resulting in enhanced image clarity and enabling a precise understanding of image content. However, it is important to exercise caution during aggressive TTA adaptation, as this may result in the introduction of artifacts or distortions that have the potential to negatively impact downstream analyses such as microscopy, remote sensing, and surveillance.

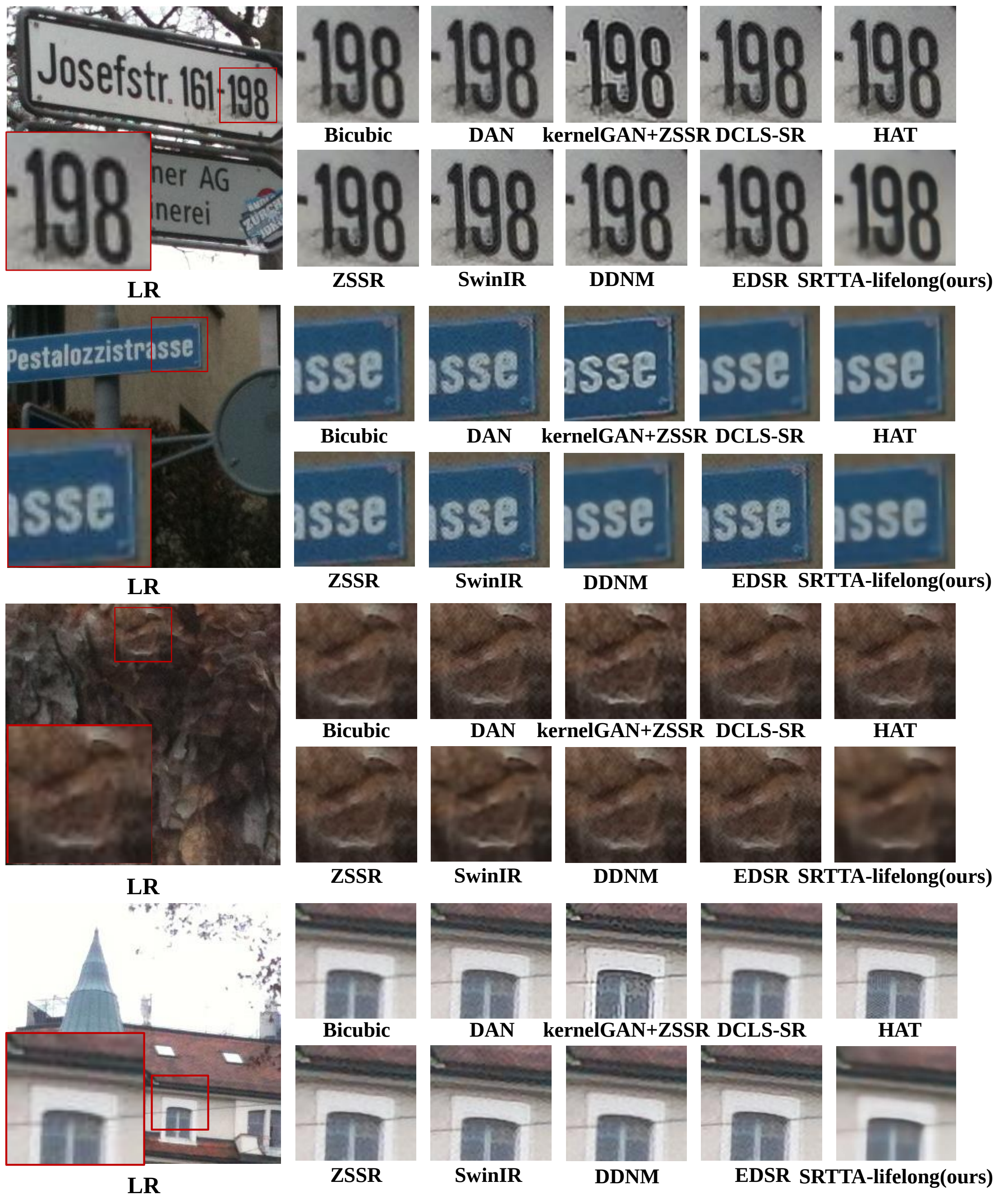

Figure F: Visualization comparison of different methods on real-world test images from DPED [13].

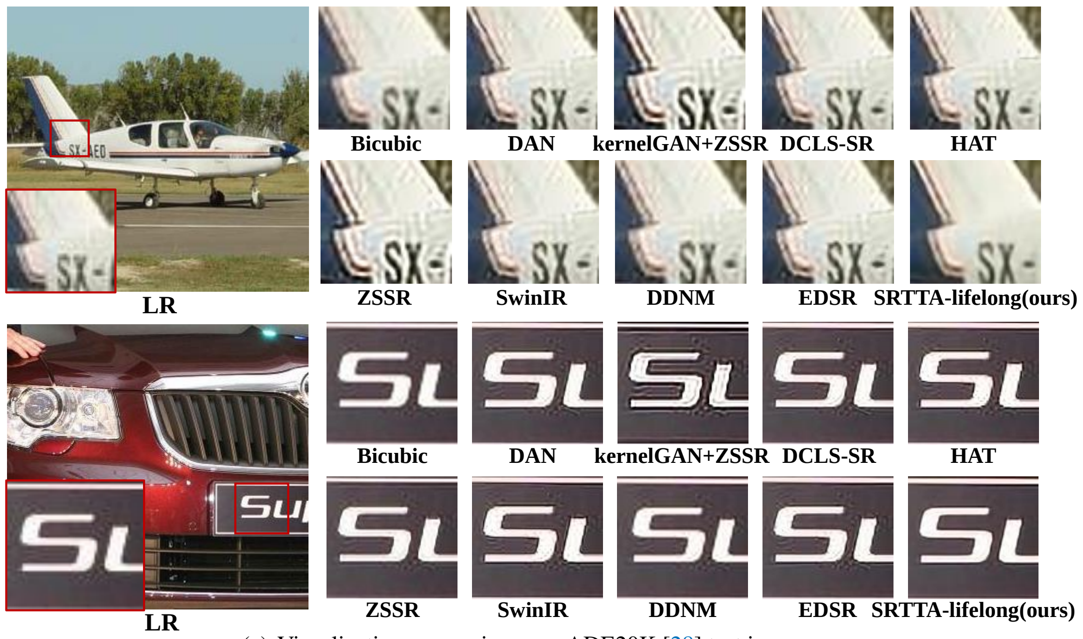

(a) Visualization comparisons on ADE20K [28] test images.

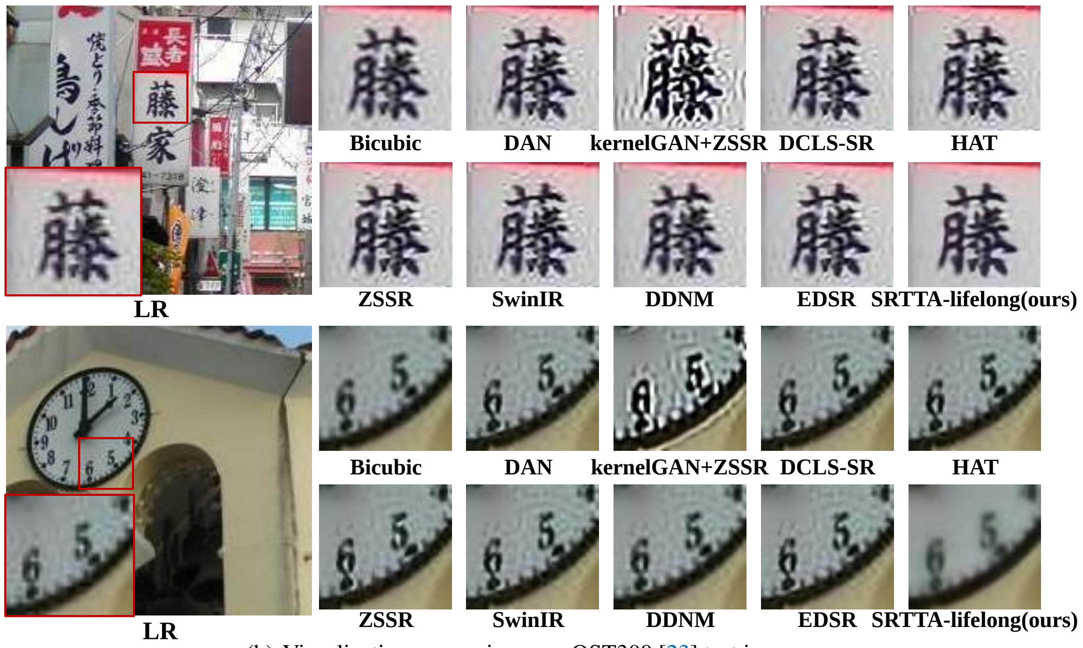

(b) Visualization comparisons on OST300 [23] test images.

Figure G: Visualization comparison on real-world test images from for 2× SR.

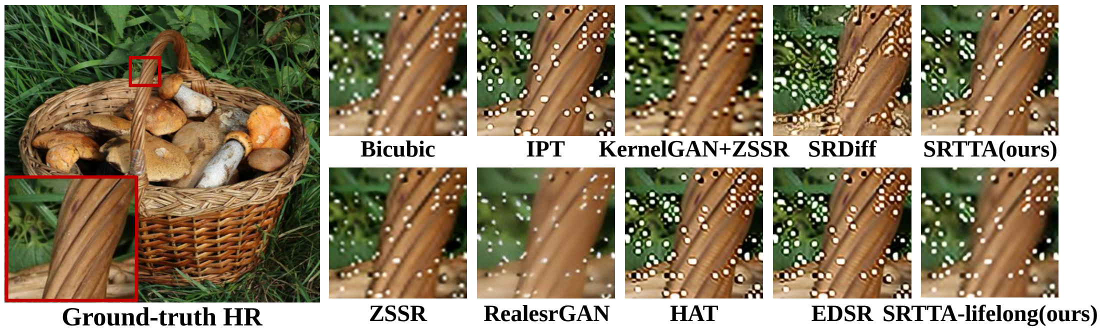

(a) Limitation visualization under Impulse Noise.

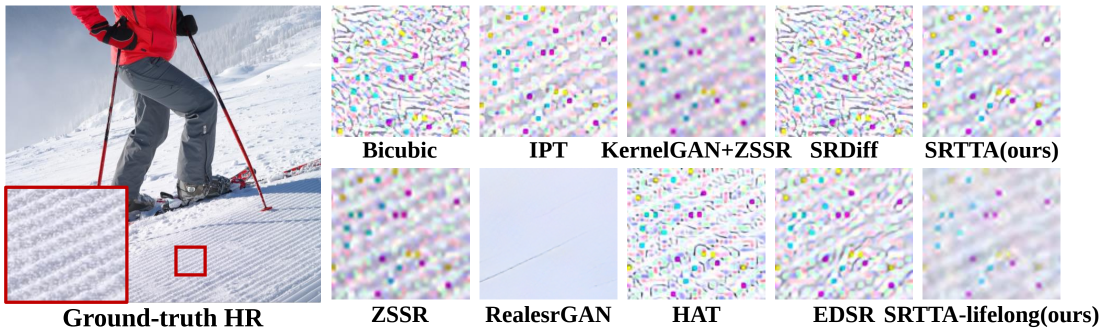

(b) Limitation Visualization under Impulse Noise.

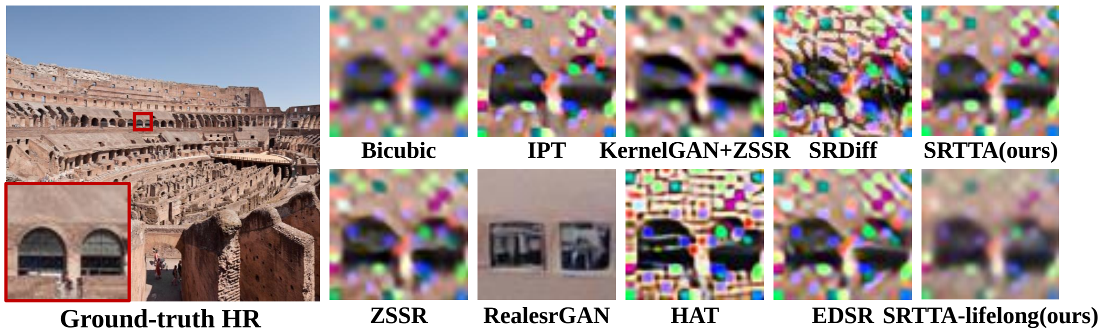

(c) Limitation visualization under Impulse Noise.

Figure H: Limitations visualization on DIV2K-C test images with degradation for 4× SR.

References

[1] S. Bell-Kligler, A. Shocher, and M. Irani. Blind super-resolution kernel estimation using an internal-gan. In *Advances in Neural Information Processing Systems*, volume 32, 2019.

[2] M. Bevilacqua, A. Roumy, C. Guillemot, and M. L. Alberi-Morel. Low-complexity single-image super-resolution based on nonnegative neighbor embedding. In *British Machine Vision Conference*, pages 1–10. BMVA press, 2012.

[3] T. Brooks, B. Mildenhall, T. Xue, J. Chen, D. Sharlet, and J. T. Barron. Unprocessing images for learned raw denoising. In *Proceedings of the IEEE/CVF Conference on Computer Vision and Pattern Recognition*, pages 11036–11045, 2019.

[4] J. Cai, H. Zeng, H. Yong, Z. Cao, and L. Zhang. Toward real-world single image super-resolution: A new benchmark and a new model. In *Proceedings of the IEEE/CVF International Conference on Computer Vision*, pages 3086–3095, 2019.

[5] H. Chen, Y. Wang, T. Guo, C. Xu, Y. Deng, Z. Liu, S. Ma, C. Xu, C. Xu, and W. Gao. Pre-trained image processing transformer. In *Proceedings of the IEEE/CVF Conference on Computer Vision and Pattern Recognition*, pages 12299–12310, 2021.

[6] X. Chen, X. Wang, J. Zhou, Y. Qiao, and C. Dong. Activating more pixels in image super-resolution transformer. In *Proceedings of the IEEE/CVF Conference on Computer Vision and Pattern Recognition*, pages 22367–22377, 2023.

[7] X. Cheng, Z. Fu, and J. Yang. Zero-shot image super-resolution with depth guided internal degradation learning. In *European Conference on Computer Vision*, pages 265–280. Springer, 2020.

[8] M. Emad, M. Peemen, and H. Corporaal. Dualsr: Zero-shot dual learning for real-world super-resolution. In *Proceedings of the IEEE/CVF Winter Conference on Applications of Computer Vision*, pages 1630–1639, 2021.

[9] D. Glasner, S. Bagon, and M. Irani. Super-resolution from a single image. In *Proceedings of the IEEE/CVF International Conference on Computer Vision*, pages 349–356. IEEE, 2009.

[10] K. He, X. Zhang, S. Ren, and J. Sun. Deep residual learning for image recognition. In *Proceedings of the IEEE conference on computer vision and pattern recognition*, pages 770–778, 2016.

[11] D. Hendrycks and T. Dietterich. Benchmarking neural network robustness to common corruptions and perturbations. In *International Conference on Learning Representations*, 2019.

[12] Y. Huang, S. Li, L. Wang, T. Tan, et al. Unfolding the alternating optimization for blind super resolution. In *Advances in Neural Information Processing Systems*, volume 33, pages 5632–5643, 2020.

[13] A. Ignatov, N. Kobyshev, R. Timofte, K. Vanhoey, and L. Van Gool. Dslr-quality photos on mobile devices with deep convolutional networks. In *Proceedings of the IEEE/CVF International Conference on Computer Vision*, pages 3277–3285, 2017.

[14] H. Li, Y. Yang, M. Chang, S. Chen, H. Feng, Z. Xu, Q. Li, and Y. Chen. Srdiff: Single image super-resolution with diffusion probabilistic models. *Neurocomputing*, 479:47–59, 2022.

[15] J. Liang, J. Cao, G. Sun, K. Zhang, L. Van Gool, and R. Timofte. Swinir: Image restoration using swin transformer. In *Proceedings of the IEEE/CVF International Conference on Computer Vision*, pages 1833–1844, 2021.

[16] B. Lim, S. Son, H. Kim, S. Nah, and K. Mu Lee. Enhanced deep residual networks for single image super-resolution. In *Proceedings of the IEEE Conference on Computer Vision and Pattern Recognition Workshops*, pages 136–144, 2017.

[17] P. Liu, H. Zhang, Y. Cao, S. Liu, D. Ren, and W. Zuo. Learning cascaded convolutional networks for blind single image super-resolution. *Neurocomputing*, 417:371–383, 2020.

[18] Z. Luo, H. Huang, L. Yu, Y. Li, H. Fan, and S. Liu. Deep constrained least squares for blind image super-resolution. In *Proceedings of the IEEE/CVF Conference on Computer Vision and Pattern Recognition*, pages 17642–17652, 2022.

[19] S. Schulte, M. Nachtegael, V. De Witte, D. Van der Weken, and E. E. Kerre. A fuzzy impulse noise detection and reduction method. *IEEE Transactions on Image Processing*, 15(5):1153–1162, 2006.

[20] A. Shocher, N. Cohen, and M. Irani. “zero-shot” super-resolution using deep internal learning. In *Proceedings of the IEEE/CVF Conference on Computer Vision and Pattern Recognition*, pages 3118–3126, 2018.

[21] Q. Wang, O. Fink, L. Van Gool, and D. Dai. Continual test-time domain adaptation. In *Proceedings of the IEEE/CVF Conference on Computer Vision and Pattern Recognition*, pages 7201–7211, 2022.

[22] X. Wang, L. Xie, C. Dong, and Y. Shan. Real-esrgan: Training real-world blind super-resolution with pure synthetic data. In *Proceedings of the IEEE/CVF International Conference on Computer Vision*, pages 1905–1914, 2021.

[23] X. Wang, K. Yu, C. Dong, and C. C. Loy. Recovering realistic texture in image super-resolution by deep spatial feature transform. In *Proceedings of the IEEE/CVF Conference on Computer Vision and Pattern Recognition*, pages 606–615, 2018.

[24] Y. Wang, J. Yu, and J. Zhang. Zero-shot image restoration using denoising diffusion null-space model. In *The International Conference on Learning Representations*, 2023.

[25] P. Wei, Z. Xie, H. Lu, Z. Zhan, Q. Ye, W. Zuo, and L. Lin. Component divide-and-conquer for real-world image super-resolution. In *Computer Vision–ECCV 2020: 16th European Conference, Glasgow, UK, August 23–28, 2020, Proceedings, Part VIII 16*, pages 101–117. Springer, 2020.

[26] K. Zhang, J. Liang, L. Van Gool, and R. Timofte. Designing a practical degradation model for deep blind image super-resolution. In *Proceedings of the IEEE/CVF International Conference on Computer Vision*, pages 4791–4800, 2021.

[27] M. Zhang, S. Levine, and C. Finn. Memo: Test time robustness via adaptation and augmentation. In *Advances in Neural Information Processing Systems*, volume 35, pages 38629–38642, 2022.

[28] B. Zhou, H. Zhao, X. Puig, T. Xiao, S. Fidler, A. Barriuso, and A. Torralba. Semantic understanding of scenes through the ade20k dataset. *International Journal of Computer Vision*, 127:302–321, 2019.

[29] M. Zontak and M. Irani. Internal statistics of a single natural image. In *Proceedings of the IEEE/CVF Conference on Computer Vision and Pattern Recognition*, pages 977–984. IEEE, 2011.